Supporting information

Fe/N/C composite in Li–O$_2$ battery: Studies of the catalytic structure and activity towards oxygen evolution reaction

Jianglan Shui,[a] Naba K. Karan,[b] Mahalingam Balasubramanian,[b] Shuyou Li[c] and Di-Jia Liu[a*]

[a] Chemical Sciences and Engineering Division and [b] X-ray Science Division , Argonne National Laboratory, Illinois 60439, and [c] Atomic and Nanoscale Characterization Experimental Center, Northwestern University, Illinois 60208, USA

1. TEM Investigation of Fe/N/C material

Transmission electron microscopy study was also carried out for Fe/N/C-HT in investigation metal particle before acid washing. Although TEM did not reveal significant difference of the sample from that of BP (**Fig. S1a**), STEM identified presence of small metal-containing crystallites (**Fig. S1b**). At higher resolution, the metal-containing particle was found to be amorphous without crystal phase (**Fig. S1c**). Such particle was identified as Fe$_3$O$_4$ by X-ray absorption spectroscopic analysis, with details given by the discussion below. After acid wash treatment, no dark particle was found in Fe/N/C-AT.
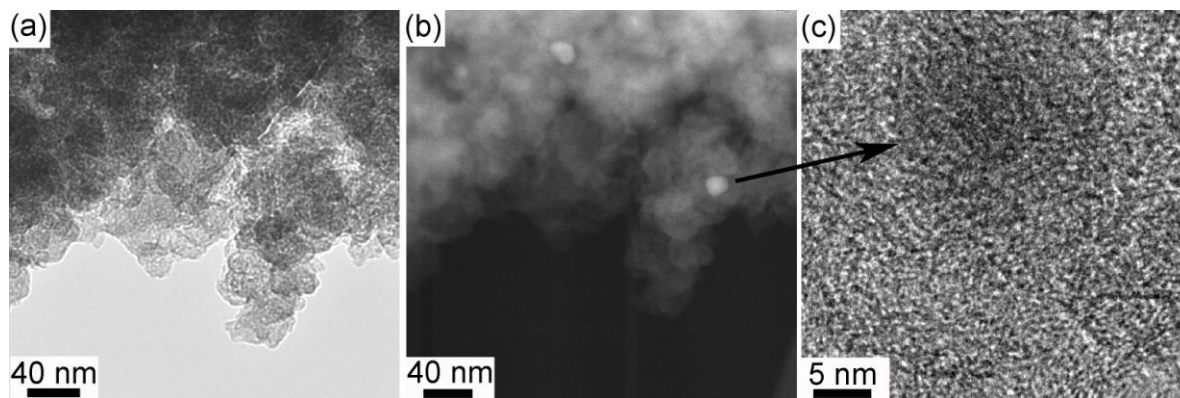

Figure S1. (a) TEM image and (b) STEM image of Fe/N/C-HT; (c) high resolution TEM image focused on a single Fe rich particle.

2. The choice of carbon papers

There are many kinds of carbon papers commercially available and they show a different degree of electrochemical activities themselves in the Li-O$_2$ cell tests. Therefore, when preparing the cathode substrate, it is important to select the type of carbon paper that produces minimum interference to the test. Some commonly used carbon papers for the electrochemical application are often preloaded with carbon nanoparticles over the carbon fibers, for example, Avcarb

carbon paper from Fuel Cell Store. **Fig. S2a** and **b** show SEM images of Avcarb at different magnification where the carbon particle layer over fiber is clearly seen. In our experiment, we chose the carbon paper which was only composed of carbon fibers, see **Fig. S2c**. **Fig. S2d** shows a side-by-side comparison of the voltage profiles between Avcarb and the regular carbon paper we used. Avcarb carbon paper produces lower overpotential than the regular one, indicating the contribution of the carbon coating. A comparative study was also performed in a multi-cycle test, as is shown by **Fig. S2e**, where Avcarb paper with preloaded carbon particles could run a number of cycles by itself in Li-O_2 batteries. Therefore, we selected spectracarb 2050A as the regular carbon paper in all our test to minimize the interference from substrates when studying the catalysts.
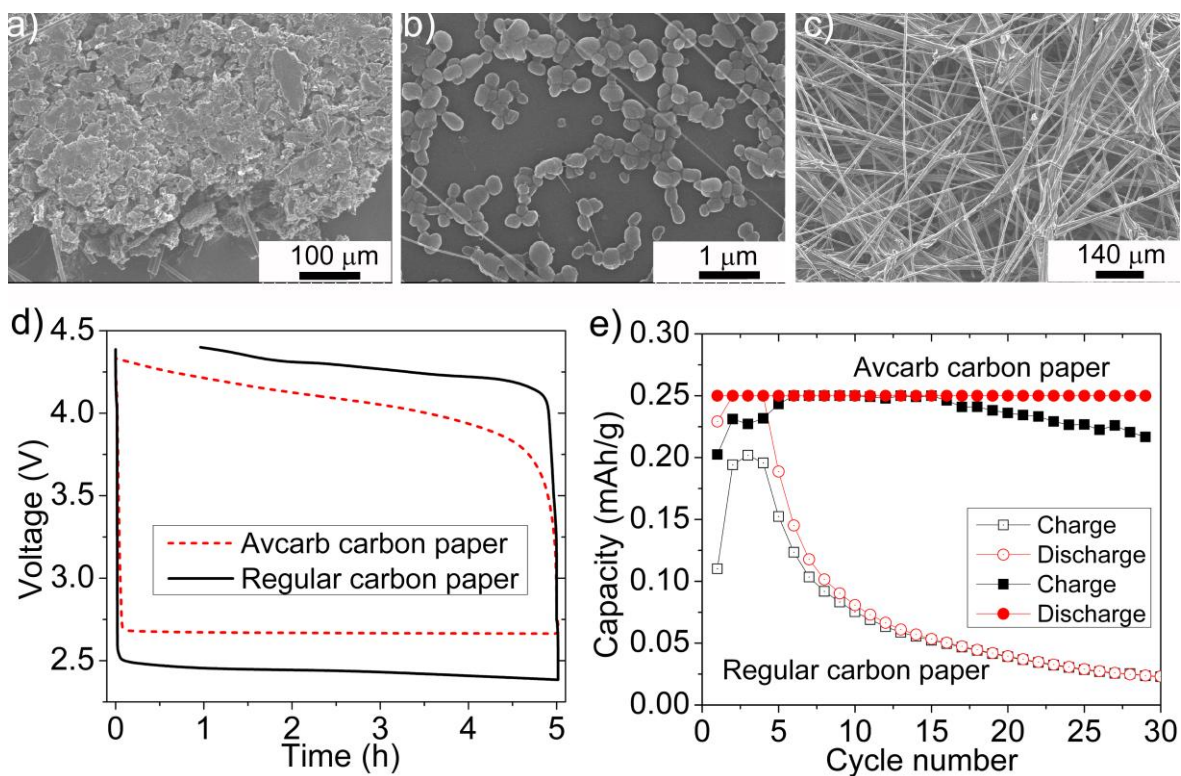

Figure S2. (a, b) SEM images of Avcarb carbon paper; (c) SEM image of regular carbon paper; (d) voltage profiles of Avcarb carbon paper and regular carbon paper; (e) cycling performances of cells using blank Avcarb carbon paper and regular carbon paper we used as cathodes. Current was 0.05 mA. Duration was set to 5 h.

3. XAS Investigation of the structure of Fe/N/C prepared at different stages in comparison with the reference compounds

XAS has been used to follow the local structural changes around Fe center accompanying the heat and acid treatment of the Fe/phen/C catalyst precursor. Some experimental details and data analysis of EXAFS and XANES data were given in the main text. The discussion in here focuses mainly on in-depth discussion of EXAFS analysis.

Prior to EXAFS analysis of the present catalyst samples, some standard sample EXAFS data were analyzed (see **Table S1** and **Fig. S3**). Various single scattering paths generated from the crystallographic information of these standards were used to fit the catalyst sample EXAFS data. Local structural parameters around Fe in Fe/N/C-AP, Fe/N/C-HT and Fe/N/C-AT samples were obtained by analyzing various peaks in Fig 2b (main text) and are given in **Table S2** and **Table S3**. Note that due to similar photoelectron scattering abilities of C, N and O, they cannot be differentiated in a particular coordination shell. Use of either N or O as back scattering atom resulted in comparable structural parameter values (note: in the fits shown below for Fe/N/C-AT and –HT samples the correlations at 1.92 and 2.2Å were modeled by N and O, respectively. Inclusion of only N and O was based on the known Fe^{+3} coordination chemistry as discussed in the main text). The average local structure around Fe in Fe(II) acetate, obtained by EXAFS analysis (using the crystallographic information as input),[1] consists of 6 O at ~2.00 Å, 6 C at ~2.95 Å and 2 Fe at ~3.33 Å. The presence of Fe-Fe correlation at ~3.33 Å is clearly evident in the EXAFS data and is in good agreement with the x ray diffraction data.

Table S1. Local structural parameters around Fe in some standard compounds obtained from analysis of various peaks in the Fourier transform (FT) magnitude of k^3 weighted Fe K-edge EXAFS. The FTs were done using a k range of 2.0-10.8 Å^{-1}. The overall amplitude reduction factor, S_0^2, was scaled to a fixed value of 0.78 for Fe. The values in the parentheses indicate the uncertainties in the last digit/s. Various bond distances for the standards from diffraction measurements have also been included in the table.

Standard/coordination shell	CN	R(Å)	σ^2(Å^2)	ΔE(eV)	R(Å)/XRD[d]
Fe(II) phthalocyanine					
Fe-N	4[a]	1.94(1)	0.0030(6)		1.93 (ref 2)
	4[a]	3.29(2)	0.0028(31)	2.4±1.5[b]	3.37 (ref 2)
Fe-C	8[a]	2.97(1)	0.0044(17)		2.96 (ref 2)
	8[a]	4.33(3)	0.0028(35)		4.21 (ref 2)
Fe(II) acetate					
Fe-O	6[a]	2.00(1)	0.0067(8)		2.14 (ref 1)
Fe-C	6[a]	2.95(7)	0.0287(168)	3.5±1.5[b]	3.17 (ref 1)
Fe-Fe	2[a]	3.33(2)	0.0068(25)		3.34 (ref 1)
Fe$_3$O$_4$					
Fe-O	1.34[a]	1.86(3)	0.0027(35)		1.89 (ref 3)
	4[a]	2.02(2)	0.0060(24)	-0.3±2.2[b]	2.06 (ref 3)
Fe-Fe	4[a]	2.98(2)	0.0085(13)		2.97 (ref 3)
	8[a]	3.48(3)	0.0065(6)		3.49 (ref 3)
	1.34[a]	3.65(7)	0.0030[c]		3.64 (ref 3)
α-Fe$_2$O$_3$					
Fe-O	3[a]	1.93(2)	0.0045(36)		1.95 (ref 4)
	3[a]	2.07(3)	0.0072(67)	0.7±1.6[b]	2.12 (ref 4)
Fe-Fe	4[a]	2.94(1)	0.0050(7)		2.95 (ref 4)
	3[a]	3.38(2)	0.0026(12)		3.36 (ref 4)
	6[a]	3.67(2)	0.0088(20)		3.71 (ref 4)

a: Coordination number (CN) values were constrained from crystallographic values. b: A single inner potential shift parameter (ΔE) was used for each fit. c: fixed intuitively. d: average distance.
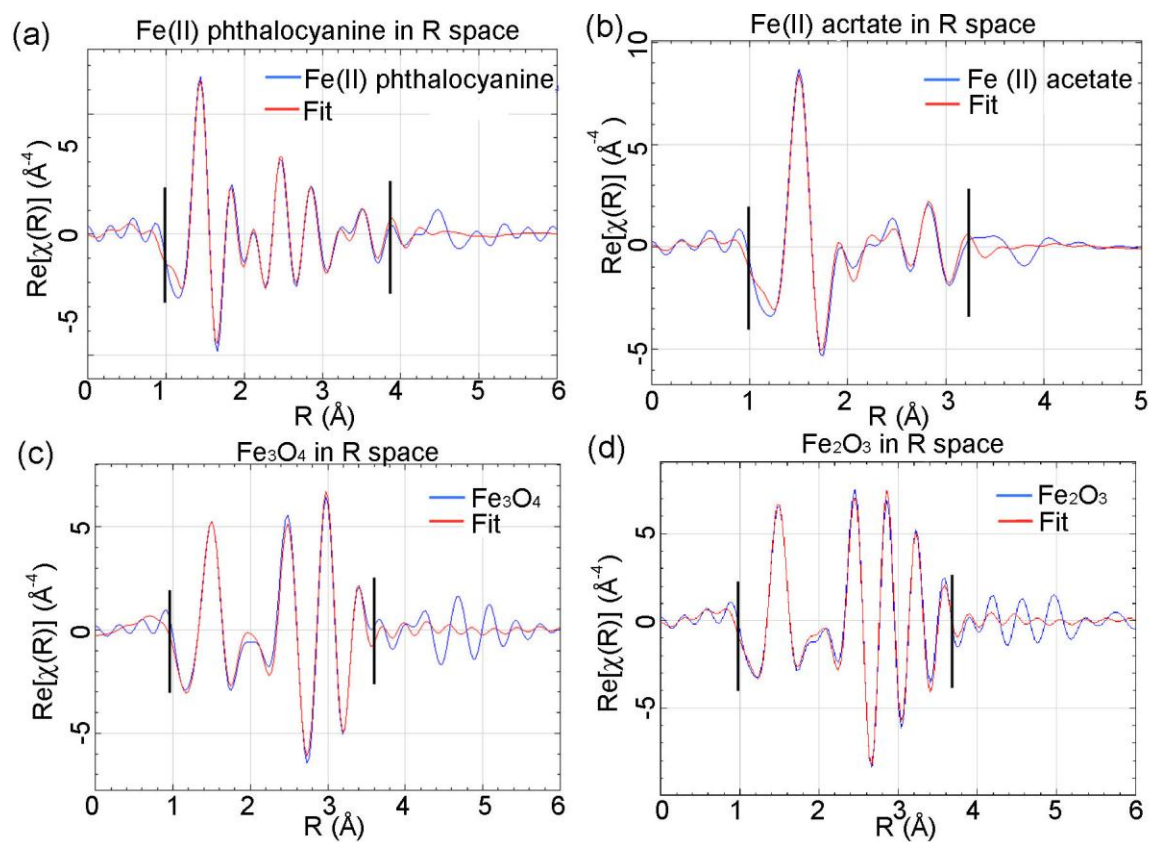
Figure S3. Real parts of FT of k^3 weighted Fe K-edge EXAFS and their fits for some standard samples. The structural parameters from these fits are given in Table S1 for these standard compounds. The vertical lines show the fit range.

Table S2. Local structural parameters around Fe in the AP, HT and AT samples obtained from the analysis of various peaks in the Fourier transform (FT) magnitude k^3 weighted Fe K-edge EXAFS. The FTs were done using a k range of 2.0-10.8 Å^{-1}. The overall amplitude reduction factor, S_0^2, was scaled to a fixed value of 0.78 for Fe. The values in the parentheses indicate the uncertainties in the last digit(s).

Sample	Coordination shell	CN	R(Å)	σ^2(Å^2)	ΔE(eV)	ΔR (Å)
AP						
	Fe-N	6[a]	1.98(1)	0.0078(6)		
	Fe-C	4[a]	2.70(4)	0.0144(42)	0.6±1.0/0.3±1.1[b]	1-3.4
		4[a]	2.95(3)	0.0100(34)		
	Fe-Fe	1[a]	3.40(2)	0.0073(26)		
AT						
	Fe-N/O	3.3±0.6	1.92[c]	0.0069(25)		1-2.05
		2.2±0.3	2.09[c]		0.1±1.2[b]	
HT						
	Fe-N/O	0.35[d]	1.86[e]	0.0034(15)[f]		
		3[d]	1.92[e]	0.0049(11)	0.3±0.8[b]	1-3.5
		1[d]	2.02[e]	0.0034(15)[f]		
		1.5[d]	2.09[e]	0.0034(15)[f]		
	Fe-Fe	1[d]	2.98(1)	0.0065(14)[g]		
		2[d]	3.49(1)	0.0065(14)[g]		
		0.35[d]	3.72(6)	0.003[h]		

a: Coordination numbers (CN) were constrained assuming 2 phen units around Fe. b: A single inner potential shift parameter (ΔE) was used for each fit. c: fixed from initial fits d: The CNs were weighted average from 75% AT sample and 25% Fe_3O_4 contribution. e: bond distances were constrained from AT sample and Fe_3O_4. f: while varied independently they were quite similar, so in the final fit they have been constrained to be the same. g: while varied independently they were quite similar, so in the final fit they have been constrained to be the same. h: fixed from Fe_3O_4.

Table S3. Comparison of local structural parameters obtained from EXAFS analysis of the Fe/N/C-AT sample using various ways of constraining the parameters during fitting. The fits were performed using the similar procedure employed as in Table S2. The values for Fe/N/C-AT sample in Table S2 are taken from fit 3 in Table S3. The parameters with quoted uncertainties were varied during the fit.

Fit	CN (Fe-N/O)	R(Å)	σ^2(Å^2)	ΔE(eV)	χ_r^2
1	4	1.92(2)	0.0084(15)	-1.2±2.4	11
	2	2.09(3)	0.0061(22)		
2	3.6(9)	1.92	0.0070(28)	-0.8±1.9	7
	1.9(5)	2.09	0.0048(34)		
3	3.3(6)	1.92	0.0069(25)$^\#$	0.1±1.2	5.7
	2.2(3)	2.09	0.0069(25)$^\#$		

- disorder for both correlations were constrained to be the same.

Fe/N/C-AP sample

The formation of Fe-phen complex in the Fe/N/C-AP sample (as evidenced by XANES and EXAFS) has previously been attributed to the color change of the solution while preparation using Fe(II) acetate and phenthroline as precursors.[5] However, the local structure of Fe-phen complex in the Fe/N/C-AP sample has not been discussed earlier. During initial analysis the coordination numbers (CNs) of various shells (1-2.75 Å) were fixed to crystallographic values in mononuclear Fe-phen complexes[6,7] and three bond distances were identified: at ~1.98 Å (Fe-N), at ~ 2.70 Å (Fe-C) and at ~2.94 Å (Fe-C)). Presence of Fe-C correlation at ~2.70 Å in the Fe/N/C-AP sample [which is absent in Fe(II) acetate] suggested the formation of Fe-phen complex. Visual inspection of the real part of the FT (see **Fig. S4**) suggested that the peak at ~3.0 Å in the Fe/N/C-AP sample could arise from Fe-Fe single scattering. A comparison of the analysis of this feature for iron(II) acetate and Fe/N/C-AP sample showed that this particular feature in Fe/N/C-AP sample arises due to Fe-Fe correlation [see **Fig. S5(a)-(c)**]. Resulting Fe-Fe bond distance was ~3.40 Å, which is slightly larger than that found in Fe(II) acetate. This is consistent with Fe-N distance (in the first coordination shell) of ~ 1.98 Å and structural integrity of the phen unit. A schematic of possible structure around Fe in Fe/N/C-AP (solid) sample is shown in **Fig. S5(d)**. Based on the structural model shown in Fig. S5(d), CNs for both Fe-C correlations (at ~2.70 and 2.94 Å) in the final fit were constrained, somewhat arbitrarily, to 4 assuming 2 phen unit around Fe. The particular choice of CNs for the Fe-C correlations, however, does not affect the conclusion about the presence of a Fe-Fe correlation in Fe/N/C-AP sample. Further characterization of the solution chemistry and the structural evolution of the precursor are ongoing to fully understand the structure of the Fe/N/C-AP sample.
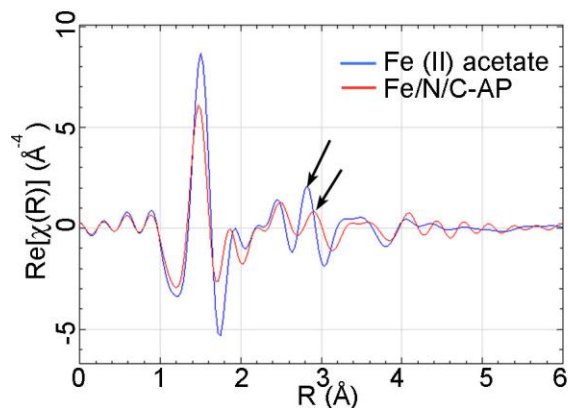
Figure S4. Comparison of real part of the FT of k^3 weighted Fe EXAFS for Fe(II) acetate and Fe/N/C-AP sample. The features of interest are marked by arrow. For Fe(II) acetate this feature indicates Fe-Fe correlation (at ~ 3.3 Å). For the Fe/N/C-AP sample this feature could suggest of Fe-Fe correlation. Figure S5(a)-(c) illustrate the evaluation and assignment of this feature arising from Fe-Fe correlation.
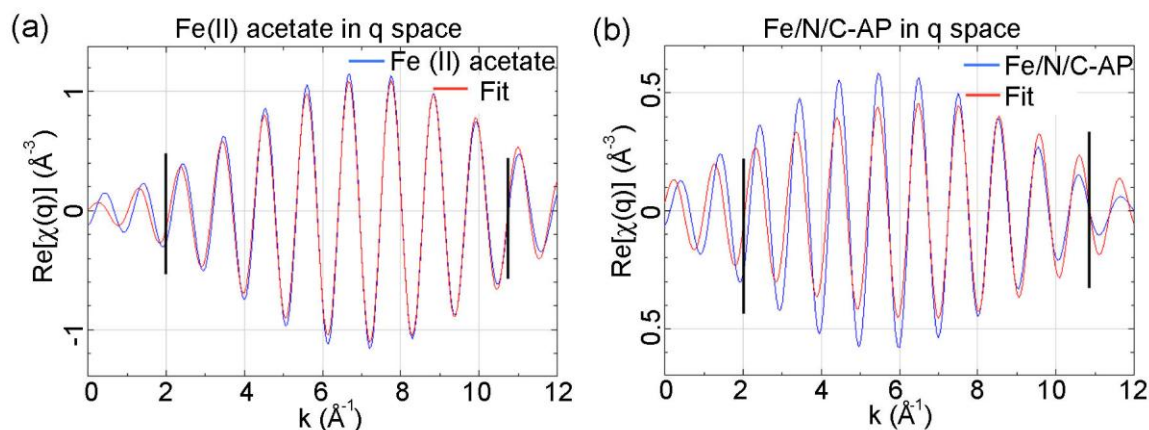

Figure S5(a, b). Comparison of experimental and fitted Fourier filtered EXAFS contribution (k^3 weighted) of the peak in the region 2.6-3.2 Å for Fe(II) acetate (S5a) and in the range 2.8-3.4 Å for Fe/N/C-AP sample (S5b). The vertical lines show k range used for Fourier transform. The fit was done using a Fe-Fe single scattering path and keeping the parameters associated with other coordination shells fixed from initial fits. The qualitatively similar envelop profiles suggest that the particular peak ~3 Å for Fe/N/C-AP sample arises due to the same backscattering atom as in Fe(II) acetate. From crystallographic information the peak ~3 Å in Fe(II) acetate arises due to Fe-Fe single scattering. Therefore, the peak ~3 Å in Fe/N/C-AP sample contains mostly Fe-Fe contribution. Moreover, the EXAFS signal strength due to this correlation for Fe(II) acetate is almost twice to that of Fe/N/C-AP sample in the entire k range, suggesting that there is 1 Fe-Fe correlation in Fe/N/C-AP sample [as there are two Fe-Fe correlations in Fe(II) acetate].
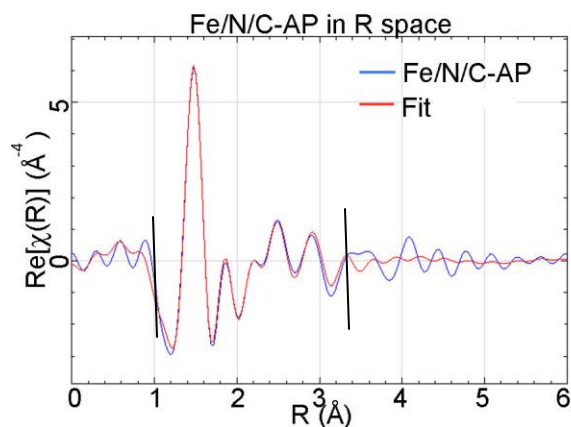
Figure S5(c). Real part of FT of k^3 weighted Fe EXAFS of Fe/N/C-AP sample along with the fit using Fe-N and two Fe-C and one Fe-Fe shells (see text). The vertical lines show the fit range.
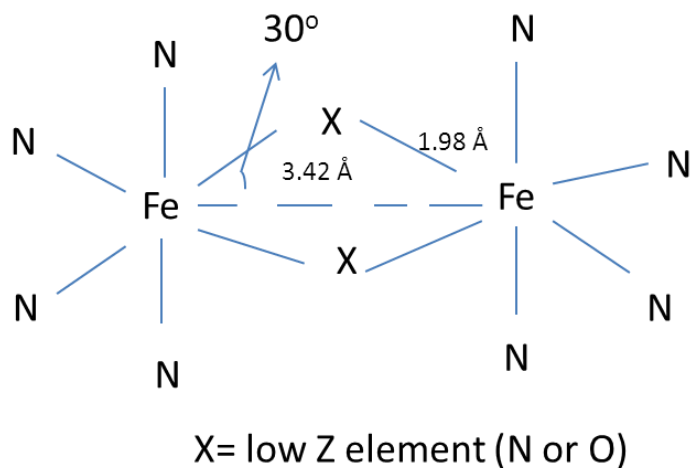

Figure S5(d). Schematic of the possible structure around Fe in Fe/N/C-AP (solid) sample based on the presence of a Fe-Fe correlation at ~ 3.4 Å.

Fe/N/C-HT and -AT samples

From the general EXAFS appearance of Fe/N/C-HT sample peaks in Figure 2(b) (main text) it can be concluded that heat treatment of the catalyst precursor in Ar environment did not result in the formation of elemental Fe clusters (to within ~2 atomic % after comparing the intensity of the peak at ~4.3 Å of elemental Fe to those of Fe/N/C-HT and Fe/N/C-AT samples) or iron carbide. This observation is in agreement with previous XAS results on catalyst system using phenanthroline, where it was also found from EXAFS analysis that there was no iron in

elemental form after heat treatment of the catalyst precursor in Ar atmosphere.[8] Note that Fe/N/C-HT sample has substantially stronger peaks between 2.2-3.6 Å compared to Fe/N/C-AP and Fe/N/C-AT samples. This observation suggested the presence of some inorganic component (iron oxide) in Fe/N/C-HT sample. A comparison of Fourier filtered EXAFS contribution (see **Fig. S6**) of the peaks in the region 2.15-3.5 Å for Fe/N/C-HT sample to that of some standards showed that Fe/N/C-HT sample contains ~25-30% iron oxide (containing predominantly Fe^{3+}). Further, linear combination of XANES using Fe/N/C-AT sample and Fe_3O_4/γ-Fe_2O_3 as standards also resulted in ~30% iron oxide phase in the Fe/N/C-HT sample (see **Fig. S7**). Note that the exact nature of the iron oxide phase could not be ascertained from the linear combination analysis. Use of Fe_3O_4 and γ-Fe_2O_3 as standards in XANES linear combination analysis does not guarantee the presence of only these phases, other forms of iron oxide could also be present. Therefore, the higher intensity peaks ~2.2-3.6 Å for Fe/N/C-HT sample mainly arises due to single scattering involving heavier element (Fe) from iron oxide phase. Additionally, absence of such strong peaks in Fe/N/C-AT sample suggested that acid treatment removed the iron oxide phase from the Fe/N/C-HT sample, which is in agreement with the STEM results. Also note that heat and acid treatment of the Fe/N/C-AP sample substantially reduced the first peak intensity. The observed substantial reduction of the first peak intensity (with concomitant asymmetric broadening) for Fe/N/C-HT and Fe/N/C-AT samples could arise from increasing disorder or from reduction of first shell coordination number or both. It could also arise from the presence of two distinctly different Fe-low Z (C/N/O) bond distances contribution to this peak. The local Fe coordination scenario with one Fe-low Z and two Fe-low Z bond distances in Fe/N/C-HT and Fe/N/C-AT samples are presented below.
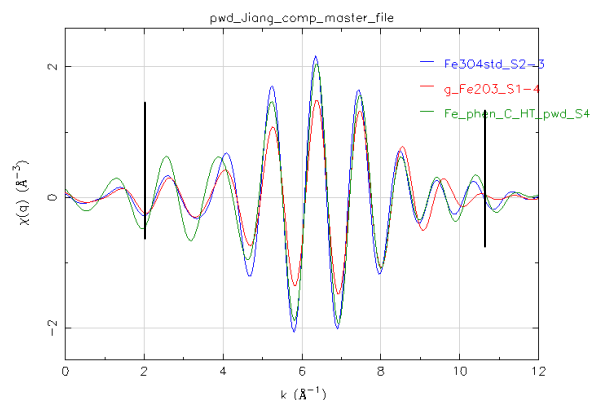

Figure S6. Comparison of Fourier filtered contribution (real part, k^3 weighted) of the peaks in the region 2.15-3.5 Å for Fe/N/C-HT sample to that of iron oxide standards. The vertical lines show k range used for Fourier transform. The amplitudes of Fe_3O_4 and γ-Fe_2O_3 spectra have been scaled to 30% for comparison. Qualitative similarity (in phase) of the Fe/N/C-HT and iron oxide data suggests that Fe/N/C-HT sample contains ~ 30% iron oxide. The mismatch (particularly at low k) arises due to some Fe-C contribution from the non-oxide part of Fe/N/C-HT sample.
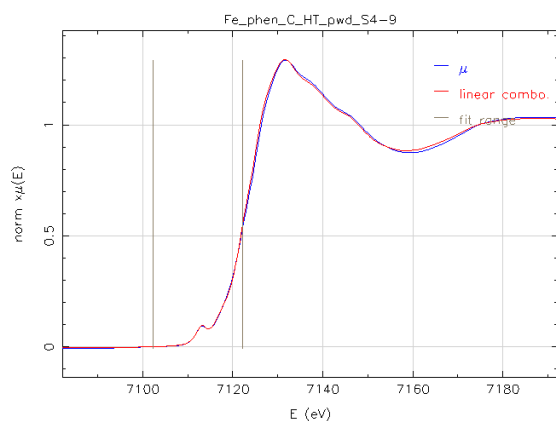
Figure S7. Representative linear combination of XANES of Fe/N/C-HT sample using Fe_3O_4, γ-Fe_2O_3 and Fe/N/C-AT sample as standards. This fit (particularly in the pre-edge region) suggests that there is substantial amount of iron oxide (~30%, containing predominantly Fe^{3+}) in the Fe/N/C-HT sample. Note that the exact nature of the iron oxide phase could not be ascertained from the linear combination analysis. Use of Fe_3O_4 and γ-Fe_2O_3 as standards in XANES linear combination analysis does not guarantee the presence of only these phases, other forms of iron oxide could also be present.

The EXAFS analysis of Fe/N/C-AT sample is presented first due to the added complexity in EXAFS analysis of the HT sample because of the iron oxide phase. Analysis of the first peak for Fe/N/C-AT sample using a single distance Fe-low Z correlation did not sufficiently reproduce the experimental data. Addition of a second Fe-low Z correlation (at different distance) significantly improved the fit as judged by the goodness of fit parameter, $χ_r^2$ (see **Fig. S8**). Note that the EXAFS data is bandwidth limited and minimum resolvable distances (Δr) involving similar backscattering atoms is given by, $Δr=π/2k_{max}$. With k_{max} of 10.8 Å^{-1} in the present case, minimum resolvable Δr between similar backscattering atoms is ~0.15 Å. The observed difference between two Fe-low Z distances (~0.17 Å) for the Fe/N/C-AT sample falls within the resolving limit. Significant improvement of the fit with two Fe-low Z distances over that with single Fe-low Z distance substantiates the presence of two Fe-low Z (C/N/O) bond distances within the first coordination shell of Fe/N/C-AT sample. Note that while modeling the first peak, the present data did not allow varying the coordination numbers; therefore they were left fixed intuitively in the initial fits. In order to get an estimate of the CNs, the bond lengths were fixed (from the initial fits) and the CNs were varied in the subsequent fits. Table S3 compares the structural parameters obtained by constraining the disorders of the two Fe-N/O correlations in different ways. Within the given $χ_r^2$, fit 2 and fit 3 (Table S3) cannot be differentiated and therefore the CNs cannot be determined with greater accuracy for the present data. Therefore, the average local structure around Fe in the Fe/N/C-AT sample is coordinated to 5-6 atoms (3.3±0.6 C/N/O at ~ 1.92 Å and 2.2±0.3 C/N/O at ~2.09 Å. Note that correlations at 1.92Å were modeled by N and correlations at 2.2Å were modeled by O). It can be said conclusively from the present analysis is that there are Fe-C/N/O contributions with two bond distances and the local

S11

coordination around Fe is not square planar, which is in agreement with the XANES results (see main text). The correlation at 2.09 Å presumably arises from axial Fe-O linkage.[9,10]
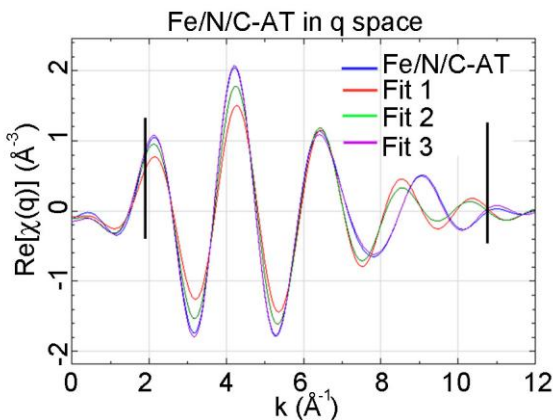

Figure S8. Fourier filtered contribution of the first peak (1-2.05 Å) to the EXAFS of Fe/N/C-AT sample. The vertical lines show k range used for Fourier transform. Fit 1 and fit 2 were done using a single Fe-N/O bond distance with coordination number fixed to 4 and 6, respectively. Fit 3 was done using 4 Fe-N/O bonds at ~1.92 Å and 2 Fe-O/N bonds at ~2.09 Å. The goodness of fit parameter χ_r^2 for fit 1, fit 2 and fit 3 were 169, 62 and 11, respectively. The addition of a second Fe-O/N correlation distance significantly improved the fit as suggested by χ_r^2 (visually as well), which demonstrated that the first coordination shell of Fe/N/C-AT sample has contributions from Fe-N/O correlations at two different bond lengths.

Analysis of the first peak of Fe/N/C-HT sample was guided by the XANES linear combination and comparison of EXAFS, which qualitatively showed that there is ~25-30% iron oxide in the Fe/N/C-HT sample. Therefore, the coordination numbers and bond distances of various Fe-N/O paths used to fit the first peak of Fe/N/C-HT sample was constrained by weighted average of contributions coming from Fe_3O_4 (used to model iron oxide) and Fe/N/C-AT samples. The features at ~2.2-3.6 Å in the Fe/N/C-HT sample were fitted with three Fe-Fe single scattering paths, whose coordination numbers were also scaled according to 25% Fe_3O_4. Any possible contribution from Fe-C correlation ~3 Å arising from the non-oxide part of the Fe/N/C-HT sample was not included in the fits assuming that the scattering involving heavier Fe would contribute more than that involving lighter C. The fit using three Fe-Fe correlations sufficiently reproduces the observed data in the range 2.2-3.6 Å for the Fe/N/C-HT sample (see **Fig. S9**) resulting in Fe-Fe distances of ~ 2.97 Å, ~3.50 Å and ~ 3.71 Å, which are in good agreement with those found in Fe_3O_4 and γ-Fe_2O_3 (2.98 Å, 3.48 Å and 3.66 Å, respectively).
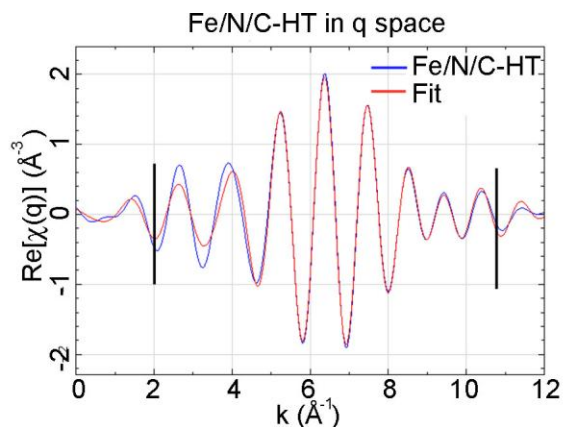
Figure S9. Fourier filtered contribution (k^3 weighted) of the peaks in the region 2.15-3.5 Å to the EXAFS of Fe/N/C-HT sample. The vertical lines show k range used for Fourier transform. The fit was done with three Fe-Fe single scattering correlations and their coordination numbers were scaled to 25% of respective values in Fe_3O_4 (suggested by linear combination of XANES in Fig S7). Mismatch of the fit at lower k, probably, arises due to not including any Fe-C correlation. The resulting Fe-Fe bond distances were comparable to those in Fe_3O_4, which further showed that Fe/N/C-HT sample contains substantial amount of iron oxide (Fe_3O_4).

4. Details on GC sampling and analysis

The preparation of cell for analysis of oxygen generated during the charging step through GC is already discussed in the main text. Briefly, the cells were firstly discharged for 10 or 5 hours in O_2 atmosphere before the oxygen was completely flushed out by ultrahigh purity (UHP) helium. Before charging step, the gas samples were taken from the cell to be analyzed by GC to ensure that no oxygen was present. The charging process started after the oxygen was completely removed and stopped after reaching pre-determined charging depths (10 or 5 hours). After the discharge, battery chamber contains mainly helium mixed with O_2 produced by oxygen evolution reaction. We followed the standard protocol for portable GC gas sampling and analysis. Briefly, a GC syringe with sample lock (25 ml, Hamilton) was used to take gas sample (15ml) from the cell (170 ml). Syringe was first flushed multiple times with UHP helium before being filled with He. We then placed the needle tip next to the sampling rubber plug, starting to push out the helium while gradually piecing through the plug. The needle was pushed into cell with 10 ml He remained in syringe, which was then injected into the cell to generate a slightly positive cell pressure. After brief moment to reach equilibrium, 15 ml sample gas from the cell was pulled into the syringe and locked in. We then transport the syringe and connected it to GC's manual injection port. Before starting the standard injection which usually would be sufficient for such protocol, we added another UHP He purge between the injection port and the syringe to drive away any residual air might be trapped in the tubing space. After He purging, the 15 ml sample gas was completely flushed through the sampling port and the very last segment was automatically sampled into the GC column when the analysis started. Generally, the sample is free of N_2 background, an indication of no air leakage. Occasionally, very low N_2 was detected by GC and corresponding O_2 was then subtracted from the GC analysis. Such correction was generally less than 2% of total oxygen value. The GC signal retention time and intensity were calibrated with the reference gases with known oxygen and CO_2 concentrations. The GC signal intensity was integrated under each peak and the percentage concentration was determined by calibrating against the known concentration in the reference. The measured quantity reported in Table 1 was derived by multiplying the percentage concentration with the total cell volume plus 10 ml helium.

The predicated O_2 production listed in Table 1 was calculated as the following: In an ideal Li-O_2 battery, lithium peroxide formation (discharge) and decomposition (charge) can be described by the equation below;

$Li^+ + O_2 + 2e \leftrightarrow Li_2O_2$
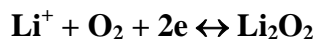
For the battery cycling under the controlled discharge/charge, the total number of electron N (mol) transferred in the charge or discharge can be calculated by dividing total electric charge of the reaction Q with the Faraday constant F. For example, for the cell operated at 0.5 mAh during charging,

$N = Q/F = 0.5*0.001*3600/96,485 = 1.866 \times 10^{-5}$ (mole)

Since each oxygen molecule requires loss of two electrons from the peroxide, the calculated volume of the O_2 produced (*V*) listed in Table 1 is derived as;

$V = 1.866 \times 10^{-5}/2*24.04*1000 = 0.224$ ml;

For cell operated at 0.25 mAh, the calculated O_2 production is 0.112 ml.

Note that we use molar volume of 24.04 L/mol in the calculation to reflect the experiment was conducted in our laboratory where the room temperature was maintained at 20 C.

5.   GC and XRD measurements on a cell after 50 cycles

Formation of O_2 through the OER of lithium peroxide was found to be the dominating process during charging over the multiple cycle study. Even at the 50th cycle where the decay of the cell performance started to accelerate, the major component in the charging gas effluent was still oxygen, as is shown by Fig. S10. Meanwhile, the formation of CO_2 was also detected. The discussion on root cause of CO_2 appearance is given in the main text.
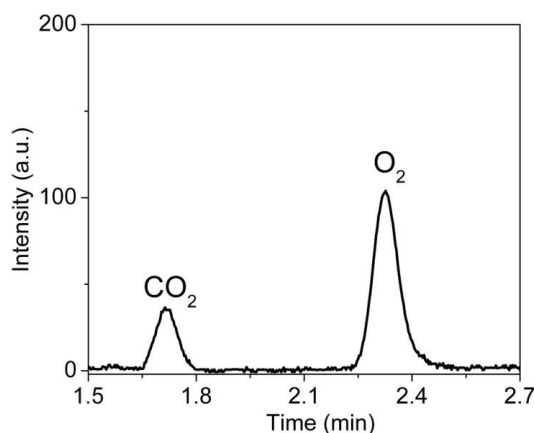

Figure S10. GC signals as the function of retention time for the gas effluents collected at the end of the 50th charging cycle from the cell with Fe/N/C as cathode catalyst. The amounts of O_2 and CO_2 were calculated as 0.059 ml and 0.013 ml, respectively.

To confirm that the reversible Li_2O_2 decomposition remained dominant process observed from the GC analysis, we also carried out a X-ray diffraction (XRD) study on the Fe/N/C cathode at the end of the 50 cycle experiment. Briefly, the cell was subjected to an additionl 36 hour discharge following the multi-cycling experiment and the cathode was studied by XRD. Fig. S11 shows clearly the formation of lithium peroxide after the discharge in comparison with

the reference XRD of Li_2O_2. The cell was then subjected to a re-charging step following the discharge. XRD shows that peaks associated with Li_2O_2 disappeared.
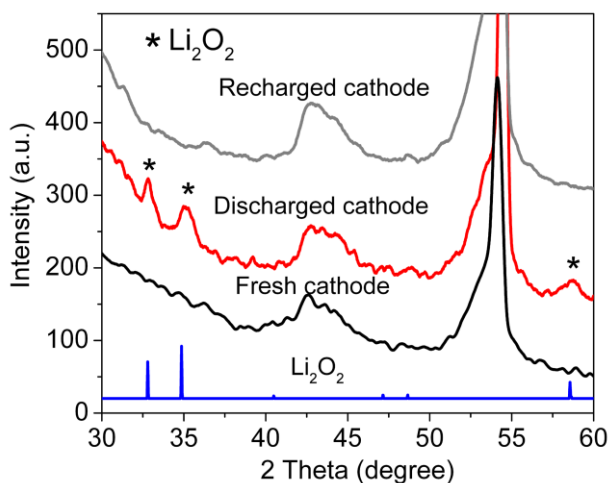

Figure S11. XRD of the Fe/N/C cathode after 36-hour discharge at 0.05 mA to 2.4 V following the 50-cycle test (middle); and XRD of the recharged cathode sample with charging voltage up to 4.5 V using with the same current of 0.05 mA.

6. Cell tested under "deep" discharge-charge condition.

To compare with the controlled capacity cycling experiment, the cell with Fe/N/C catalyst was also subjected to a "deep" discharge-charge testing condition. Fig. S12 shows the load curve of the cell, together with those from the reference cells in which α-MnO$_2$/XC-72 or BP was used as the cathode catalyst. In this experiment, the battery was first discharged to 2.2 V in 95 hours at current intensity of 0.05 mA. The cell was then flushed out by UHP He and charged up to 4.5 V in helium. The gas effluent generated by the cell with Fe/N/C cathode at the end of charge was collected and analyzed by GC, as described by the discussion below.

The cell with Fe/N/C cathode possessed lower overpotentials under both discharge and charge condition than the references. One could view Fig. S12 as consisted of both catalyzed and non-catalyzed electrochemical processes. The initial stage of discharge may be interpreted as controlled by catalytic ORR with formation of Li_2O_2 as the dominant product near Fe/N/C active site. Beyond this point, other non-catalytic process could also occur and Li_2O_2 could form on the undecorated carbon surface. During the recharging, the catalytic decomposition of Li_2O_2 near the active site has a lower reaction barrier and should occur first. The charging voltage by the catalyzed (Fe/N/C) process, therefore, is significant lower than the non-catalyzed (BP) one. At the charging step below 50%, both catalyzed and un-catalyzed decompositions may occur on the carbon surface. At potential above 4 V, not only Li_2O_2 but also electrolyte could undergo decomposition. Therefore both O_2 and CO_2 were expected in the gas effluent.
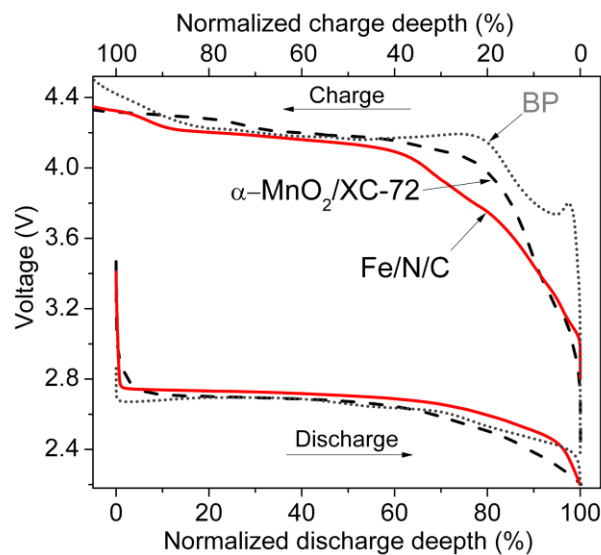
Figure S12. (a) Discharge/charge voltage profiles of Li-O$_2$ cells using Fe/N/C, α-MnO$_2$/XC-72 and BP as cathode catalysts. Current was 0.05 mA. Cutoff voltage was set to 2.2 V for discharge and 4.5 V for charge. The discharge-charge depth was normalized for all three batteries by taking discharge depth at 2.2 V as 100%. The specific capacity for Fe/N/C catalyst was 4320 mAh/g (1.1 mg catalyst, 4.75 mAh).

Fig. S13 showed GC signal of gas effluent collected at the end of charging step from the cell with Fe/N/C catalyst. O$_2$ was still the dominant component although a significant fraction of CO$_2$ was detected. Compared with CO$_2$-free results under limited discharge and low charging potential, as described in the main text, we attribute the CO$_2$ production from the electrolyte decomposition occurred at charging voltage > 4 V, which is also consistent with the reports by others. [11, 12]
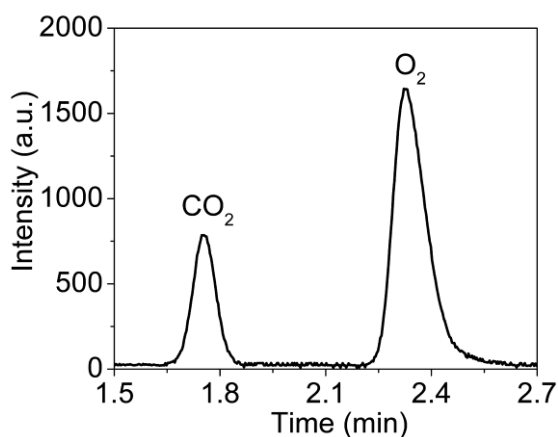

Figure S13. GC signals for the gas effluents collected from the cell with Fe/N/C as cathode catalyst at the end of the charging step according to Fig. S12. The analysis showed that 1.203 ml of O$_2$ and 0.282 ml of CO$_2$ were produced during the charging step.

The difference in the gas product composition and the overpotential between controlled and "deep" discharge/charge could be explained by the following proposed catalytic mechanism: Our characterization study showed that the catalytic centers in Fe/N/C are atomically distributed throughout the support of carbon (BP). Since Fe/N/C site is known to bind with O_2 selectively to lower ORR activation barrier [Ref 41 – 45], Li_2O_2 is expected to preferentially formed near the active site over the carbon surface under a capacity-controlled discharge. Such Li_2O_2 precipitated near Fe/N/C site will readily undergo the decomposition during OER in the charging step. Since both ORR and OER are promoted by the catalytic site, we observed reduced overpotentials in the discharge as well as the recharge steps, as are shown by Fig. 5 in the main text. However, when the battery undergoes a high-capacity, or "deep" discharge, the active sites will be saturated by Li_2O_2 first. The excess Li_2O_2 has to be deposited over the less-active carbon surface. For these Li_2O_2 precipitates, the electrochemical behavior during charging should not be much different from that found in the comparative BP sample. Therefore, the charging behavior after a "deep" discharge should really be consisted of the contribution from both catalytically promoted (near active site) and unpromoted (on carbon surface) reactions. The catalytic promoted reaction should occur first due to a lower reaction barrier, followed by the unpromoted reaction. This appears to be what we found in Fig. S12. During the charge step, the cell with Fe/N/C catalyst showed a significantly lower overpotential than that with only-BP material in the first 50% of the charging span before the two voltage curves were nearly merged together. Since most of the unpromoted reaction occurred at charging potential over 4 V, a significant production of CO_2 was expected, as we observed in Fig. S13.

Based on this proposed mechanism, an electrocatalyst with complete coverage of active site (in the absence of non-active carbon) should provide a near-complete reversibility of ORR/OER for Li_2O_2 with little negative impact to the electrolyte. In a very recent report, Peng et al. reported nearly 95% capacity retention and up to 100 cycle of a Li-O_2 battery using a pure nanoporous gold cathode.[13] They observed the complete reversibility of Li_2O_2 formation-decomposition with little side reaction to electrolyte (DMSO). Such study suggested an exciting possibility for future research of Fe/N/C-liked catalyst for Li-air battery. If one could populate the catalyst surface with a substantially higher amount of, if not completely, the active site to overshadow the non-active carbon, one should be able to achieve a low-cost and high capacity catalyst with good reversibility and lifespan.

References

1. B. Weber, R. Betz, W. Bauer, and S. Schlamp, Z. Anorg. Allg. Chem., 637, 102 (2011).

2. P. Coppens and L. Li, J. Chem. Phys., 81, 1983 (1984).

3. B. A. Wechsler, D. H. Lindsley and C. T. Prewitt, Am. Mineralo., 69, 754 (1984).

4. R. L. Blake, R. E. Hessevick, T. Zoltai and L. W. Finger, Am. Mineral., 51, 123 (1966).

5. M. Lefèvre, E. Proietti, F. Jaouen and J. P. Dodelet, Science, 324, 71 (2009).

6. V. C. R. Payne, R. T. Stibrany and A. A. Holder, Analytical Sci., 23, 169 (2007).

7. L. L. Koh, Y. Xu and A. K. Hsieh, Acta. Cryst., C50, 884 (1994).

8. M. Bron, J. Radnik, M. F. Erdmann, P. Bogdanoff and S. Fiechter, J. Electroanal. Chem., 535, 113 (2002).

9. S. Kim, T. Ohta and G. Kwag, Bull. Korean Chem. Soc., 21, 588 (2000).

10. W. R. Scheidt, I. A. Cohen and M. E. Kastner, Biochemistry, 18, 3546 (1979).

11. S. A. Freunberger, Y. Chen, N. E. Drewett, L. J. Hardwick, F. Bardé and P. G. Bruce, Angew. Chem. Int. Ed. 50, 8609 (2011).

12. B. D. McCloskey, R. Scheffler, A. Speidel, D. S. Bethune, R. M. Shelby and A. C. Luntz, J. Am. Chem. Soc., 133, 18038 (2011).

13. Z. Q. Peng, S. A. Freunberger, Y. H. Chen and P. G. Bruce, Science, 337, 563 (2012).